ADVANCED ENERGY MATERIALS
www.advenergymat.de

A Stabilized, Intrinsically Safe, 10% Efficient, Solar-Driven Water-Splitting Cell Incorporating Earth-Abundant Electrocatalysts with Steady-State pH Gradients and Product Separation Enabled by a Bipolar Membrane

Ke Sun, Rui Liu, Yikai Chen, Erik Verlage, Nathan S. Lewis, and Chengxiang Xiang**

A water-splitting cell consists of two electrolyte-containing compartments: a cathode compartment in which protons and/or water molecules are reduced to H_2(g), and an anode compartment in which hydroxide ions and/or water molecules are oxidized to O_2(g). The compartments are bridged by a membrane that provides the ionic transport necessary to complete the oxidation-reduction circuit while maintaining separation of the products. Laboratory-scale demonstrations of sunlight-driven water splitting typically use cells that have the same electrolyte in the cathode and the anode compartments.[1] Intrinsically safe electrolyzers do not produce potentially explosive mixtures of H_2(g) and O_2(g) at any point in space or time in the reactor. A cation-exchange membrane (CEM) such as Nafion, or an anion-exchange membrane (AEM) such as a SELEMION membrane, are typically used with strongly acidic or strongly alkaline electrolytes, respectively, to provide proton or hydroxide-ion transport and high ionic conductivities, while minimizing crossover of the product gases.[2] The unity transference number for protons or hydroxide ions in solar-fuels cells that include a CEM or an AEM and a strongly acidic or strongly alkaline electrolyte (pH 0 or 14) minimizes the voltage lost due to resistance, pH gradients, and electrodialysis and obviates the need to actively manage salts in the system. In contrast, when used with electrolytes of near-neutral pH, CEMs, or AEMs result in electrodialysis of the solution that ultimately prevents the cell from operating.[3]

The need to utilize the same electrolyte on both the anode and cathode sides of the cell imposes constraints on the stability and compatibility of the light absorbers and electrocatalysts in the system. For example, Si and transition-metal phosphides allow the pairing of an acid-stable photocathode with a highly active, earth-abundant, acid-stable electrocatalyst for the hydrogen-evolution reaction (HER). However, for acidic electrolytes, a complementary pairing is not currently available for a stable photoanode with a highly active, earth-abundant, stable, electrocatalyst for the oxygen-evolution reaction (OER).[4]

Bipolar membranes consist of a layered structure of a CEM joined to an AEM, and in principle allow for the use of different electrolytes in the anolyte and catholyte of a solar-driven water-splitting cell.[5,6] BPMs are widely used in industrial electrodialysis processes to separate anions from cations in a salt solution, with charge balanced by the splitting of water molecules to produce protons and hydroxide ions at the interface. The BPMs promote the dissociation of water at the interface between the CEM and AEM sides of the membrane, and thereby allow a pH difference between the anolyte and catholyte to be maintained at steady state.[5,7] BPMs consequently offer prospects for relaxing materials-compatibility constraints, increasing options for electrolytes, and enabling new designs for water-splitting cells. Previous feasibility studies have shown that the use of BPMs, such as fumasep FBM, in water-splitting cells with steady-state differences of 0–14 pH units or 0–7 pH units allowed for sustained operation of such systems.[5,8]

We report herein a sustained, intrinsically safe, 10% efficient, solar-driven water-splitting cell based on CoP/H_2SO_4 (aq, pH = 0)/BPM/KBi (aq, pH 9.3)/Ni/TiO_2/InGaP/GaAs. Detailed experimental procedures are provided in the Supporting Information. The nonphotoactive cathode consisted of either a Pt mesh or a Ti mesh that had been coated with a CoP HER catalyst.[9] The cathode was connected electrically to a tandem-junction photoanode (GaAs/InGaP) that had a GaAs bottom cell (E_g = 1.42 eV) and an InGaP top cell (E_g = 1.84 eV), which was designed for illumination by the AM 1.5 solar spectrum.[2] The top of the GaAs/InGaP photoanode was coated by a 62.5 nm thick layer of amorphous TiO_2 grown by atomic-layer deposition (ALD) at 150 °C, with tetrakis(dimethylamido)titanium and water as precursors.[2,10] The thickness of the TiO_2

Dr. K. Sun, Dr. R. Liu, Y. Chen, E. Verlage, Prof. N. S. Lewis, Dr. C. Xiang
Joint Center for Artificial Photosynthesis
California Institute of Technology
Pasadena, CA 91125, USA
E-mail: nslewis@caltech.edu; cxx@caltech.edu
Dr. K. Sun, Prof. N. S. Lewis
Division of Chemistry and Chemical Engineering
210 Noyes Laboratory
127-72, California Institute of Technology
Pasadena, CA 91125, USA
E. Verlage
Department of Applied Physics and Materials Science
California Institute of Technology
Pasadena, CA 91125, USA
Prof. N. S. Lewis
Beckman Institute and Molecular Materials Research Center
California Institute of Technology
Pasadena, CA 91125, USA
Prof. N. S. Lewis
Kavli Nanoscience Institute
California Institute of Technology
Pasadena, CA 91125, USA

DOI: 10.1002/aenm.201600379

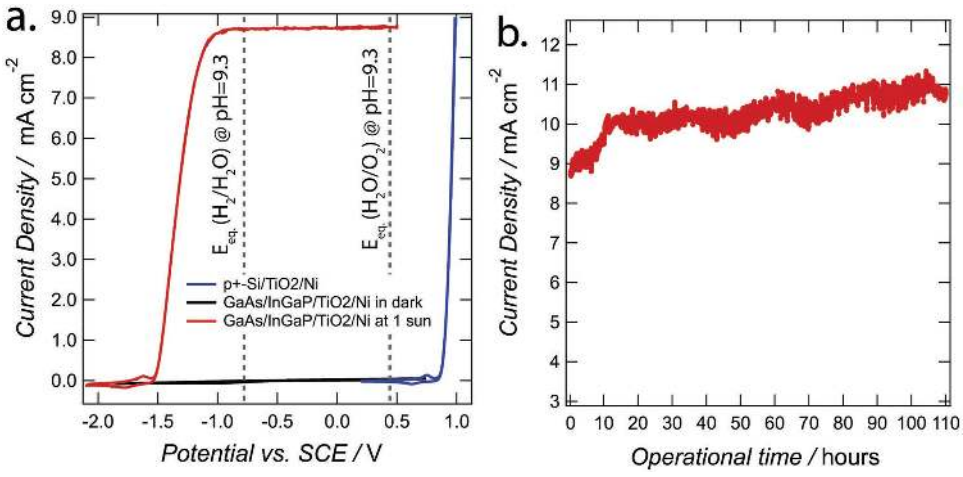

Figure 1. a) Cyclic voltammetry of a freshly prepared GaAs/InGaP/TiO_2/Ni photoanode in contact with a 0.5 M potassium borate buffer solution (KBi) at pH 9.3 in the dark (black) and under 1 sun of simulated solar illumination (red). The current density versus potential (*J*–*E*) characteristic for a non-photoactive p^+-Si/TiO_2/Ni electrode effecting the oxygen-evolution reaction under the same conditions is shown in blue. The equilibrium potentials at pH 9.3 for the oxygen-evolution reaction (OER) and the hydrogen-evolution reaction (HER) are indicated by the dotted lines. b) The photocurrent density, J_{photo}, as a function of operational time for a GaAs/InGaP/TiO_2/Ni photoanode biased potentiostatically to –0.016 V versus a reversible hydrogen electrode (RHE) (blue dotted line in Figure 1a).

protective layer was optimized by optical modeling to minimize the reflection loss at the water/dielectric layer interface.[2] A layer of Ni metal (≈2 nm thick) was sputter-deposited onto the TiO_2 surface, and served both as an ohmic contact to the solution and as an OER catalyst.[2,4,10] The catholyte was 1.0 M H_2SO_4 (aq, pH 0) and the anolyte was a 0.5 M potassium borate solution (KBi, pH 9.3). The two electrolytes were separated by a bipolar membrane (fumasep FBM).

Figure 1a shows the current density versus potential (*J*–*E*) behavior of a 0.23 cm^2 tandem-junction GaAs/InGaP/TiO_2/Ni photoanode in contact with the KBi solution, both in the dark and under simulated 1 sun illumination. For comparison purposes, Figure 1a also shows the *J*–*E* behavior of the OER using the TiO_2/Ni layers deposited onto a nonphotoactive p^+-Si substrate (p^+-Si/TiO_2/Ni), where the amorphous TiO_2 layer provided ohmic contacts with low contact resistance to the degenerately doped semiconductor as well as to the Ni metal catalyst. After correction for uncompensated resistance, an overpotential of ≈660 mV was required to drive the OER at a rate corresponding to 10 mA cm^{-2} of current density, using the activated thin Ni metal catalyst in contact with the 0.5 M KBi solution. Hence, the Ni metal catalyst required the application of an additional ≈300 mV overpotential when operated in KBi relative to the overpotential required to drive the OER at the same current density and catalyst loading in 1.0 M KOH(aq).[2] A load-line analysis based on an equivalent-circuit model consisting of a photovoltaic component connected in series with a dark electrolysis cell (see Supporting Information for detailed calculation) allows the extraction of the photovoltaic behavior by subtracting the dark p^+-Si/TiO_2/Ni electrode *J*–*E* behavior from the behavior of the GaAs/InGaP/TiO_2/Ni photoanode. This analysis resulted in a photovoltaic component with a performance equivalent to that produced by a GaAs/InGaP tandem cell with an open-circuit voltage (V_{oc}) of 2.37 V, a short-circuit current density (J_{sc}) of 8.7 mA cm^{-2}, and a fill factor (*FF*) of 84.8%, hence exhibiting a photovoltaic (PV) efficiency of 16.3%. The V_{oc} obtained from the load-line analysis was consistent with the solid-state and photoelectrochemical measurements conducted under 100 mW cm^{-2} AM 1.5 solar illumination previously reported for the GaAs/InGaP device.[2]

Figure 1b shows the photocurrent density as a function of time for a GaAs/InGaP/TiO_2/Ni photoanode biased potentiostatically at the formal potential for the OER (–0.016 V versus a reversible hydrogen electrode, RHE) while in contact with 0.5 M KBi(aq) and illuminated by a halogen lamp at 1 sun, in a three-electrode configuration with a standard calomel reference electrode (SCE) and a Pt mesh counter electrode. The photocurrent density at this applied bias, J_{photo} (–0.016), increased from 9.0 to 10.5 mA cm^{-2} during the 100 h test. After the 100 h stability test (see Figure S2 in Supporting Information), the photoanode exhibited negligible change in onset potential or equivalent open-circuit voltage relative to the beginning of the test. The increase in J_{photo} (–0.016), particularly during the first 20 h of operation, may reflect changes in the refractive index and/or optical absorptivity of the Ni layer due to electrochemically induced changes in the morphology and thickness of the layer.[11]

Figure 2a shows a schematic illustration of the BPM-containing cell, in which the anolyte was 0.5 M KBi(aq) and the catholyte was 1.0 M H_2SO_4(aq). Dissociation of water at the AEM–CEM interface within the BPM releases hydroxide ions and protons, which migrate into the anolyte and catholyte, respectively. When the rate of water dissociation in the BPM is equal to the rate of consumption of the protons and hydroxide ions at the electrode surfaces, a steady-state pH gradient is maintained. Figure 2b shows chronoamperometric (CA) data for a two-electrode BPM-containing cell using a 1.06 cm^2 area photoelectrode, a ≈4.5 cm^2 BPM, and a Ti mesh/CoP counter electrode under 100 mW cm^{-2} of simulated solar illumination, with no external bias (Figure S1, Supporting Information). The Ti/CoP cathode was prepared as described previously[9] with details provided in the Supporting Information, and under these conditions exhibits a quantitative faradaic yield for H_2(g) evolution.[9]

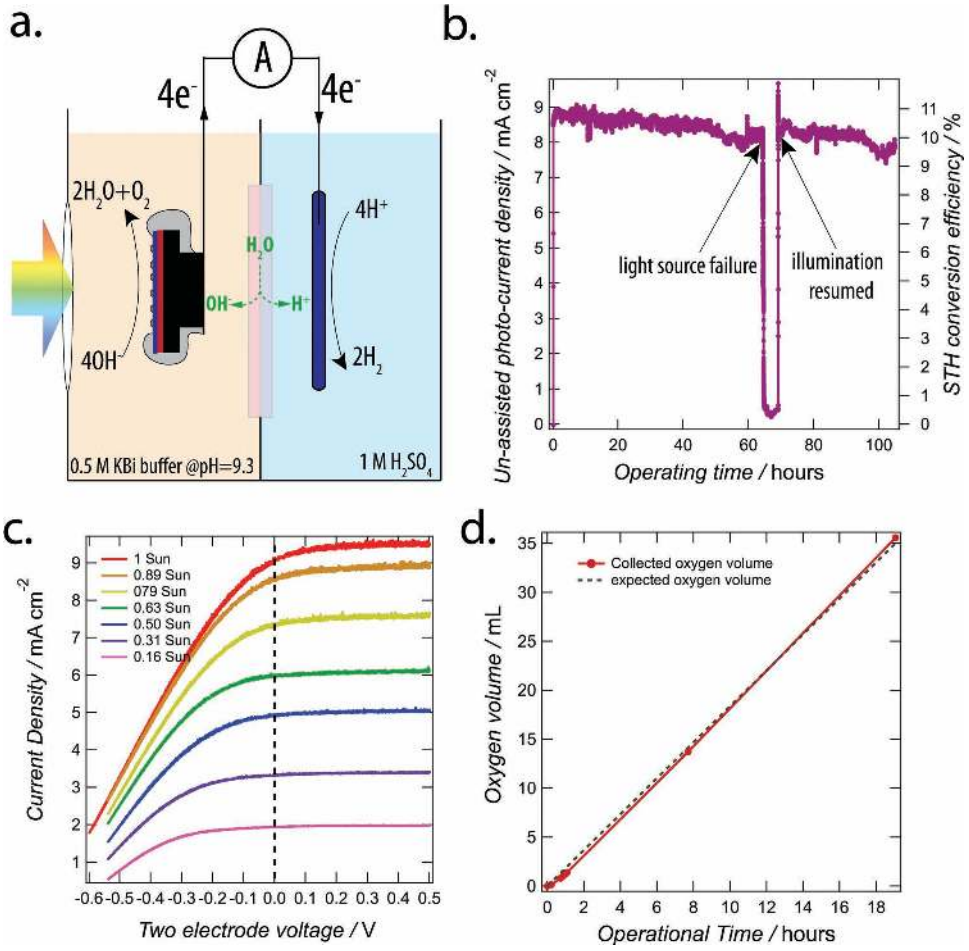

Figure 2. a) Schematic illustration of a spontaneous solar-driven water-splitting system that incorporates a bipolar membrane (BPM) to maintain steady-state pH gradients. b) The photocurrent density and corresponding solar-to-hydrogen conversion efficiency, η_{STH}, observed during unassisted water splitting using a BPM-containing GaAs/InGaP/TiO_2/Ni cell in a two-electrode configuration incorporating a CoP/Ti mesh cathode and under 1 sun of simulated solar illumination from a halogen lamp. The light source failed after ≈70 h of operation and illumination was resumed ≈5 h later. c) Photocurrent density as a function of voltage applied between the GaAs/InGaP/TiO_2/Ni photoanode and a CoP/Ti mesh cathode at a range of illumination intensities. The short-circuit condition (i.e., with no applied bias) is indicated by the dotted black line. d) The volume of oxygen produced as a function of time, as determined from gas-collection measurements (solid red line), and the volume of oxygen that would be produced based on the current passed as a function of time assuming 100% Faradaic efficiency for oxygen evolution (dotted line).

The electrocatalytic performance of the Ti/CoP cathode was separately characterized in a three-electrode electrochemical setup in 1.0 M H_2SO_4 (aq), and an overpotential of ≈100 mV was observed at a cathodic current density of 10 mA cm^{-2} for the HER, comparable to previous observations for CoP (see Figure S7, Supporting Information). At the beginning of the measurement, $J_{photo}(0)$ was 8.2 mA cm^{-2}, which corresponds to a solar-to-hydrogen (STH) conversion efficiency, η_{STH}, of 10.0%. The current density and efficiency of this cell were lower than the performance expected from the short-circuit photocurrent density observed using smaller area (≈0.2 cm^2) photoelectrodes (Figure 1), with the difference in performance for cells using the larger (1.06 cm^2) photoelectrode most likely resulting from the additional overpotential for the HER as well as the increased path length for ion transport around the edge of the larger electrode, which would increase the solution-based resistance losses in the cell. Nonuniformity or defects in the junction would also be expected to have a greater effect on larger-area electrodes, because larger samples should statistically contain a greater absolute number of defects than smaller electrodes. After 100 h of operation, $J_{photo}(0)$ decreased to 7.5 mA cm^{-2}, corresponding to a 9.3% relative decrease in η_{STH} over the 100 h period. A load-line analysis was performed in which the polarization data for the water-splitting reaction were overlaid with the current density–voltage behavior of the photodiode to yield the operational current density for the unassisted solar-driven water-splitting reaction, (see Figure S3, Supporting Information). At an operational photoelectrode current density of ≈8.0 mA cm^{-2}, the kinetic overpotentials for the OER and HER in the system were ≈600 and ≈100 mV, respectively. The membrane voltage loss, $V_{membrane,loss}$, was ≈300 mV at the membrane current density (≈1.8 mA cm^{-2}) in the operating cell (**Figure 3**d). Hence, the total voltage required to drive the water-splitting cell at ≈8.0 mA cm^{-2} of photoelectrode current density was ≈1.23 + 0.6 + 0.1 + 0.3 ≈2.2 V, which was close to the photovoltage provided by the photodiode at that photocurrent

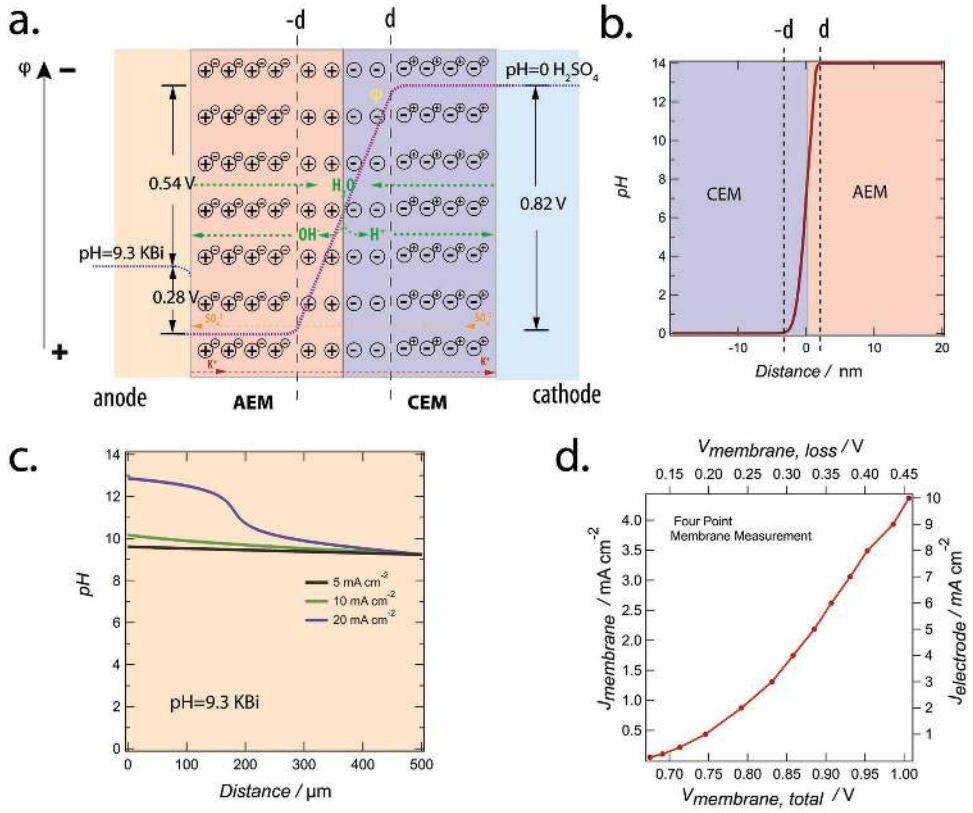

Figure 3. a) A schematic illustration of the electrochemical potentials in the KBi(aq, pH 9.3)/FUMASEP FBM/H_2SO_4(aq, pH 0) cell. b) Simulated pH profile across the AEM and CEM interface using a Poisson–Nernst–Planck model. c) Simulated pH profile at the AEM/electrolyte interface when the equivalent hydroxide flux from the AEM into the buffered electrolyte at pH 9.3 was 5, 10, or 20 mA cm^{-2}. d) Current density normalized to the membrane area (left axis) and the electrode area (right axis) as a function of the measured total membrane voltage, $V_{membrane,total}$ (bottom axis) and the membrane voltage loss, $V_{membrane,loss}$ (top axis).

density. At the current densities observed during the stability test, dissolution of the entire epilayer (InGaP/GaAs layer) of the photoelectrode at 100% Faradaic efficiency would require <2% of the total charge passed (see Supporting Information for calculation). Negligible change in the pH of the electrolyte in either compartment of the cell was expected even if the BPM exhibited a substantial leakage current, because of the relatively large volume of the anolyte (15 mL) and the catholyte (15 mL) compared to the pH change expected in those volumes if every electron passed in the circuit were accompanied by transfer of a co-cation or a co-anion through the membrane.

Figure 2c shows the current density at various illumination intensities as a function of the two-electrode bias voltage applied to the BPM-containing cell. At zero applied bias (black dotted line) and for lower illumination intensities (≤0.5 suns), $J_{photo}(0)$ approached the light-limited photocurrent density, resulting in an improvement in efficiency from η_{STH} = 9.6% under 1 sun illumination to η_{STH} = 10.4% at 0.5 sun illumination and to η_{STH} = 13.0% under 0.2 sun illumination. Under 1 sun illumination, $J_{photo}(0)$ = 7.8 mA cm^{-2} was close to the light-limited photocurrent density (8.2 mA cm^{-2}). The efficiency of the device could thus be further improved by reducing the residual voltage losses in the cell, for example, by reducing the resistive losses from the membrane or the solution resistive loss, and/or by improving the performance of the catalysts.

Figure 2d shows the volume of oxygen collected as a function of time from the anolyte, compared to the expected volume of oxygen that should be produced as a function of time based on the charge passed and assuming 100% Faradaic efficiency for oxygen evolution. A near-unity Faradaic efficiency for O_2 production at the photoanode was observed over the course of ≈20 h of continuous operation in 0.5 M KBi(aq), suggesting minimal corrosion of the GaAs/InGaP/TiO_2/Ni photoelectrode under such conditions.

Stabilization of large-area photoelectrodes for operational lifetimes sufficient to allow practical or commercial deployment of an integrated solar water-splitting system is facilitated by the use of defect-tolerant photoelectrode materials. Chemically stable oxides have exhibited long-term stability (100–1000s of h) for Si, CdTe, and InP photoanodes coated with reactively sputtered NiO_x films, but similar performance has not been observed for coated GaP and GaAs[11,12] electrodes under the same conditions. Although visible defects were typically observed on samples after 100 h of continuous operation in the BPM-containing cell (see Figure S6, Supporting Information), the improved stability of the large-area (≈1 cm^2) samples used in this work relative to previous reports, in alkaline media, is indicative of the reduced dissolution rates for the oxidized species of the GaAs, InAlP, InGaP, and AlGaAs layers in 0.5 M KBi(aq) relative to the dissolution rates of these materials in

1.0 M KOH(aq).[2,10] The anion-exchange membrane (AHA-type, NEOSEPTA membrane) used in the previous work[2] and the BPM used in this work exhibited excellent stability and were not the cause of the observed slight decrease in the device performance versus time. Pinhole formation around dust particles that were present on photoanode surface before the protection coating process was therefore likely the cause of the decrease in device performance in the 0.5 M KBi (aq) solution as well as in the 1.0 M KOH(aq) solution.

The mechanisms for enhanced water dissociation and ionic transport in a BPM have been modeled and characterized previously.[7] As shown in Figure 3, under steady-state operation, three distinctive regions, including a transition region and two bulk regions for the cation-exchange membrane and the anion-exchange membrane, exist in the BPM. In the transition region near the interface between the two ion-exchange membranes, the concentration of counter ions is reduced relative to the bulk regions, and uncompensated fixed charges are present. This region (between $-d$ and d in the illustration) is commonly referred to as the "space-charge region" in solid-state physics nomenclature. The majority of the drop in the electric potential occurs in the transition region resulting from uncompensated fixed charges, with negligible potential drops present across the two bulk regions. The potential difference across the transition region can be described by the relationship $\Delta\varphi = 2\frac{kT}{q}\ln\left(\frac{X}{C}\right)$, where X and c are the concentration of the fixed charge and the mobile species in the transition region, k is Boltzmann's constant, T is the absolute temperature, and q is the unsigned charge on an electron. Assuming a fixed charge density of 1.0 mol L^{-1} and a mobile charge concentration of 10^{-7} mol L^{-1}, the electric potential difference between the CEM and AEM is calculated to be 0.83 V. A numerical model that couples the electrostatic Poisson's equation and the Nernst–Plank equation was used to simulate the pH profile, electrochemical potential profile and the fixed charge densities in the bipolar membrane cell (see Supporting Information). Figure 3b shows the simulated pH profile across the CEM/AEM interface. The change of the proton or hydroxide concentration occurs within a few nanometers in the transition region, and the accompanying electrochemical potential difference due to the pH difference was also 0.83 V at the CEM/AEM interface. An additional potential difference, the Donnan potential, develops at the membrane/electrolyte interfaces, and can be determined by the relationship $\varphi_{Don} = \varphi_m - \varphi_s = 0.059\frac{kT}{q}\ln\left(\frac{C_s}{C_m}\right)$, where φ_m and φ_s are the electrochemical potential in the membrane and the electrolyte, respectively, and C_s and C_m are the mobile concentrations of protons or hydroxide ions at the electrolyte/BPM interface and in the ion-exchange membrane, respectively. At the pH 9.3 for the KBi/BMP interface, φ_{Don} is calculated to be 0.28 V at equilibrium. Consequently, the thermodynamic potential required to drive the water-dissociation reaction at the BPM interface at steady state is given by $V_{membrane,equilibrium}$ = 0.83 V $-\varphi_{Don,AEM} - \varphi_{Don,CEM}$, or 0.059 V × ($pH_{AEM,surface}$ − $pH_{CEM,surface}$), where $\varphi_{Don,AEM}$ and $\varphi_{Don,CEM}$ are the Donnan potential drops at the anolyte/AEM and catholyte/CEM interfaces, respectively, and $pH_{AEM,surface}$ and $pH_{CEM,surface}$ are the pH of the electrolyte at the electrolyte/AEM interface and the electrolyte/CEM interface, respectively. For the pH 9.3 KBi/pH 0 H_2SO_4 (aq) system, $V_{membrane,equilibrium}$ = 0.55 V. Hence, the chemical bias produced by the pH difference between the catholyte and anolyte that would reduce the thermodynamic potential for water splitting by 0.059 V × ($pH_{anolyte}$−$pH_{catholyte}$) = 0.55 V is cancelled by the $V_{membrane,equilibrium}$ in the cell. The BPM-containing system entails no correction for chemical bias in the system because water dissociates in the membrane, providing the steady-state source of both protons and hydroxide ions necessary to maintain the pH gradient, as opposed to dissipation of the pH gradient by recombination of protons and hydroxide to produce water and thus release energy. Equivalently, the free energy for splitting water into H_2(g) and O_2(g) is a state function, and as long as water is the only reactant consumed and there is no chemical change at steady state in either the anolyte, catholyte, or membrane, as is the case herein, the free energy for the photoelectrosynthetic reaction involving production of 1 atm of H_2(g) and 1 atm of O_2(g) from H_2O(l) under standard conditions is 1.23 V. Although the change in the local pH at the CEM/electrolyte interface was negligible even at high operating current densities, due to the high concentration and high mobility of protons in the 1.0 M H_2SO_4 (aq) solution, the local pH at the AEM/electrolyte interface was highly dependent on the water-dissociation rate at the CEM/AEM interface and on the amount of convective stirring in the cell. Figure 3c shows that at high membrane current densities (>10 mA cm^{-2}) without active stirring, the local pH at the AEM/electrolyte interface increased substantially, due to hydroxide transport from the AEM toward the borate solution. The increase in the pH at the AEM/electrolyte interface resulted in a decrease of φ_{Don} and an increase in the membrane voltage loss.

Figure 3d shows the current density as a function of the experimentally measured membrane voltage, $V_{membrane,total}$ (bottom axis) and as a function of the membrane voltage loss, $V_{membrane,loss}$ (top axis) (see Supporting Information for an illustration of the four-point experimental setup). The membrane voltage loss was given by: $V_{membrane,loss} = V_{membrane,total} - V_{membrane,equilibrium}$, where $V_{membrane,total}$ was measured from a four-point probe measurement and $V_{membrane,equilibrium}$ was 0.55 V in the anolyte/catholyte system. The left axis of the graph is the operational current density normalized to the membrane area, $J_{membrane}$, and the right axis is the operational current density normalized to the photoactive electrode area, $J_{electrode}$. The membrane area in the four-point measurement setup (see Figure S4, Supporting Information) was ≈2.3 times larger than the electrode area. From Figure 3d, at $J_{electrode}$ = 10 mA cm^{-2}, or $J_{membrane}$ = 4.36 mA cm^{-2}, $V_{membrane,loss}$ = 1.0 V–0.059 V × (9.3–0) = 0.45 V was required to drive the overall water-splitting reaction at steady state. The $V_{membrane,loss}$ largely resulted from ohmic resistance in the membrane and from the overvoltage for water dissociation in the transition region of the BPM. Due to active agitation of the solution electrolyte, the portion of the membrane voltage loss due to the pH gradient at the anolyte/CEM interface was calculated to be <100 mV. After 72 h of continuous operation at $J_{electrode}$ = 10 mA cm^{-2}, the pH of the catholyte and anolyte each changed by <0.1 pH unit. A change of >1 pH unit would have occurred had 100% of the charge passed in the system resulted in electrodialysis of the electrolytes. After passage of $J_{electrode}$ = 10 mA cm^{-2} for 72 h, the membrane voltage changed <5% relative to the value at beginning of the test.

Table 1. Ion crossover rates for the bipolar membrane as determined from ICP-MS measurements.

	J_{K^+}	$J_{SO4^{2-}}$	f_{H^+}	f_{OH^-}
$J_{membrane}$ = 0.5 mA cm^{-2}	51 μA cm^{-2}	140 μA cm^{-2}	90.0%	73.0%
$J_{membrane}$ = 4 mA cm^{-2}	110 μA cm^{-2}	318 μA cm^{-2}	97.5%	92.3%
$J_{membrane}$ = 25 mA cm^{-2}	225 μA cm^{-2}	452 μA cm^{-2}	99%	98.3%

Transport of H^+, OH^-, K^+, and SO_4^{2-} ions in the system was further characterized using inductively coupled plasma mass spectrometry (ICPMS) to measure ion concentrations in the anolyte and catholyte after passing charge through the BPM at various current densities. **Table 1** summarizes the current density corresponding to the leakage of K^+ and SO_4^{2-} across the membrane when the BPM was operated at three different $J_{membrane}$ values. Table 1 also presents the membrane selectivities, $f_{H^+} = \frac{C_{H^+}}{C_{total}}$ and $f_{OH^-} = \frac{C_{OH^-}}{C_{total}}$, where C_{total} is the total charge passed through the membrane and C_{H^+} and C_{OH^-} are the proton-carried and hydroxide-carried portions of the total charge passed, respectively. The imperfect permselectivity of the CEM and AEM in FUMASEP FBMs resulted in the transport of K^+ and SO_4^{2-} between the cathode and anode compartments. At low $J_{membrane}$, the leak current due to K^+ or SO_4^{2-} transport was relatively substantial and constituted more than 25% of the total charge transported through the FUMASEP FBM. When $J_{membrane}$ was increased above 4 mA cm^{-2}, close to the maximum $J_{membrane}$ shown in Figure 3, the membrane selectivity, f_{H^+} or f_{OH^-}, increased to >92%, and the majority of the ionic transport in the FUMASEP FBM membrane resulted from the dissociation of water within the BPM. The observed increase in the membrane selectivity at high operational current densities agrees with the limiting-current model for the co-counter ions and the reported performance of the bipolar membrane.[13] The oxygen and hydrogen permeability of the bipolar membrane was also measured experimentally. Relative to the Nafion membrane, the bipolar membrane exhibited reduced permeability for both O_2(g) and H_2(g) (Table S1, Supporting Information). The low permeability for H_2(g) and O_2(g) provides for robust gas separation and collection and insures intrinsically safe operation of the device.

In the absence of an earth-abundant catalyst for the OER that is stable in 1.0 M H_2SO_4(aq) solution, devices that use Nafion as the membrane and consequently operate in acidic electrolytes require the use IrO_x or RuO_x to provide stable, active OER electrocatalysts. The BPM device configuration investigated herein allowed instead the simultaneous use of earth-abundant electrocatalysts for the HER at pH 0 and for the OER at pH 9.3. Relative to a cell that operates in a strongly alkaline electrolyte, which also allows the use of earth-abundant electrocatalysts for both the HER and OER, the BPM-containing device produced voltage losses due to the FUMASEP FBM resistive loss, as well as electrodialysis at the FUMASEP FBM/anolyte and electrode/anolyte interfaces. Table S2 (Supporting Information) compares the various potential losses for the FUMASEP FBM configuration and the CEM configuration. The $V_{membrane,loss}$ across the BPM was 400–500 mV at $J_{membrane}$ = 4.36 mA cm^{-2} (Figure 3d) and is expected to exceed 1.0 V at $J_{membrane}$ = 10 mA cm^{-2}. The large $V_{membrane,loss}$ in the BPM and the increased overpotential for OER under near-neutral pH conditions will substantially limit the attainable η_{STH} in such a system in relative to an analogous cell that operates instead in conventional, alkaline media. Although chemical corrosion of the Ni OER catalyst at pH 9.3 with a borate buffer is reduced compared to degradation observed the presence of phosphate or bicarbonate buffers at the same pH, the oxidized Ni catalyst is nevertheless partially soluble under these conditions, and eventually soluble Ni species will either contaminate the catholyte and membrane in a confined cell, and/or will be fully removed from the anode and anolyte in a liquid flow cell configuration that uses a pure water feed. The lack of unity permselectivity across the BPM used herein will also eventually lead to electrodialysis of the solution and/or require active management of the buffer species and of the pH of the electrolytes to achieve true steady-state cell operation. Fully integrated designs in which the light absorbers are embedded in the BPM will operate under local pH conditions that are either highly alkaline or highly acidic (Figure 3), and will not benefit from the ability to buffer the local pH near the electrode surface to near-neutral values, as is possible when the cell has discrete, separated electrodes, electrolyte solutions, and membrane components (Figure 2a).

In summary, unassisted, intrinsically safe, solar-driven water splitting was demonstrated at η_{STH} = 10% for >100 h using a >1 cm^2 tandem photoelectrode and a ≈4.5 cm^2 bipolar membrane that allowed maintaining the anolyte at pH 9.3 and the catholyte at pH 0. The water-splitting efficiency displayed by the BPM-incorporated photoelectrochemical cell was equivalent to the use of a photovoltaic (PV) cell with an efficiency of 16% in series with a ≈65% efficient electrolyzer unit. The bipolar membrane prevented product gas crossover and partly impeded ion crossover during steady-state operation. Incorporation of the BPM led to an enhancement in the stability of the photoanode due to operation under passivating conditions, and enabled operation of a cell without the need to find a stable, active OER catalyst in acidic electrolytes. This specific bipolar membrane, however, introduced an additional $V_{membrane,loss}$ of 400–500 mV at $J_{membrane}$ = 4.36 mA cm^{-2} and of ≈1.0 V at $J_{membrane}$ = 10 mA cm^{-2} , would require active mass management of ions and protons to achieve a true steady-state operating condition, and would thus reduce the attainable optimal η_{STH} by at least 4–5% points relative to cells that did not possess such membrane-related voltage losses.

Supporting Information

Supporting Information is available from the Wiley Online Library or from the author.

Acknowledgements

The authors declare no competing financial interests. This material is based upon work performed by the Joint Center for Artificial Photosynthesis, a DOE Energy Innovation Hub, supported through the Office of Science of the US Department of Energy under Award Number DE-SC0004993, as well as grant number 1225 from the Gordon and Betty Moore Foundation. The authors also thank N. Dalleska (Caltech) for his assistance with measurements and analysis of the ICPMS data. The authors also thank S. Lu, K. Walczak for gas-crossover measurements,

R.J.R. Jones for designing the flow-cell reactor, X. Zhou for preparation of the ALD TiO_2 coatings, and J. C. Crompton for preparation of the CoP-coated metal meshes.

Received: February 21, 2016
Revised: March 19, 2016
Published online:

[1] O. Khaselev, J. A. Turner, *Science* **1998**, *280*, 425.
[2] E. Verlage, S. Hu, R. Liu, R. J. R. Jones, K. Sun, C. Xiang, N. S. Lewis, H. A. Atwater, *Energy Environ. Sci.* **2015**, *8*, 3166.
[3] J. Jin, K. Walczak, M. R. Singh, C. Karp, N. S. Lewis, C. Xiang, *Energy Environ. Sci.* **2014**, *7*, 3371.
[4] a) C. C. L. McCrory, S. Jung, I. M. Ferrer, S. M. Chatman, J. C. Peters, T. F. Jaramillo, *J. Am. Chem. Soc.* **2015**, *137*, 4347; b) C. C. L. McCrory, S. Jung, J. C. Peters, T. F. Jaramillo, *J. Am. Chem. Soc.* **2013**, *135*, 16977.
[5] M. B. McDonald, S. Ardo, N. S. Lewis, M. S. Freund, *ChemSusChem* **2014**, *7*, 3021.
[6] N. M. Vargas-Barbosa, G. M. Geise, M. A. Hickner, T. E. Mallouk, *ChemSusChem* **2014**, *7*, 3017.
[7] M. Ünlü, J. Zhou, P. A. Kohl, *J. Phys. Chem. C* **2009**, *113*, 11416.
[8] D. A. Vermaas, M. Sassenburg, W. A. Smith, *J. Mater. Chem. A* **2015**, *3*, 19556.
[9] F. H. Saadi, A. I. Carim, E. Verlage, J. C. Hemminger, N. S. Lewis, M. P. Soriaga, *J. Phys. Chem. C* **2014**, *118*, 29294.
[10] S. Hu, M. R. Shaner, J. A. Beardslee, M. Lichterman, B. S. Brunschwig, N. S. Lewis, *Science* **2014**, *344*, 1005.
[11] K. Sun, F. H. Saadi, M. F. Lichterman, W. G. Hale, H.-P. Wang, X. Zhou, N. T. Plymale, S. T. Omelchenko, J.-H. He, K. M. Papadantonakis, B. S. Brunschwig, N. S. Lewis, *Proc. Natl. Acad. Sci. USA* **2015**, *112*, 3612.
[12] a) K. Sun, Y. Kuang, E. Verlage, B. S. Brunschwig, C. W. Tu, N. S. Lewis, *Adv. Energy Mater.* **2015**, *5*, 1402276; b) K. Sun, M. T. McDowell, A. C. Nielander, S. Hu, M. R. Shaner, F. Yang, B. S. Brunschwig, N. S. Lewis, *J. Phys. Chem. Lett.* **2015**, *6*, 592; c) X. Zhou, R. Liu, K. Sun, D. Friedrich, M. T. McDowell, F. Yang, S. T. Omelchenko, F. H. Saadi, A. C. Nielander, S. Yalamanchili, K. M. Papadantonakis, B. S. Brunschwig, N. S. Lewis, *Energy Environ. Sci.* **2015**, *8*, 2644.
[13] a) H. Strathmann, J. J. Krol, H. J. Rapp, G. Eigenberger, *J Membr. Sci.* **1997**, *125*, 123; b) I. C. Bassignana, H. Reiss, *J. Membr. Sci.* **1983**, *15*, 27; c) P. Ramirez, H. J. Rapp, S. Reichle, H. Strathmann, S. Mafe, *J. Appl. Phys.* **1992**, *72*, 259; d) J. L. Gineste, G. Pourcelly, Y. Lorrain, F. Persin, C. Gavach, *J. Membr. Sci.* **1996**, *112*, 199.